IEEE Access
Multidisciplinary | Rapid Review | Open Access Journal

Received February 17, 2021, accepted February 26, 2021, date of publication March 2, 2021, date of current version March 25, 2021.

Digital Object Identifier 10.1109/ACCESS.2021.3063292

A Scale Normalized Generalized LoG Detector Approach for Retinal Vessel Segmentation

MOHAMMAD A. U. KHAN[1], FAIZAN ABDULLAH[2], AWAIS AKRAM[3], RIZWAN ALI NAQVI[4], MEHWISH MEHMOOD[5], DILDAR HUSSAIN[6], AND TOUFIQUE AHMED SOOMRO[7], (Member, IEEE)

[1]Department of Electrical Engineering, Namal Institute Mianwali, Mianwali 42201, Pakistan
[2]Faculty of Science Engineering & Built Environment, School of Information Technology, Deakin University, Geelong, VIC 3217, Australia
[3]Department of Primary and Secondary Healthcare, Lahore 54000, Pakistan
[4]Department of Unmanned Vehicle Engineering, Sejong University, Seoul 05006, South Korea
[5]Department of Electrical and Computer Engineering, COMSATS University Islamabad, Islamabad 45550, Pakistan
[6]School of Computational Sciences, Korea Institute for Advanced Study (KIAS), Seoul 02455, South Korea
[7]Department of Electronic Engineering, Quaid-e-Awam University of Engineering, Science and Technology, Larkana 67450, Pakistan

Corresponding authors: Dildar Hussain (hussain@kias.re.kr) and Rizwan Ali Naqvi (rizwanali@sejong.ac.kr)

This work was supported by the Korea Institute for Advanced Study, South Korea, under Grant CG076601, and in part by the Sejong University Faculty Research Fund.

ABSTRACT Retinal vessel segmentation is important for analyzing many retinal diseases, where manual segmentation of these vessels is an extensive job. Automatic segmentation of these vessels can help much in the diagnosis of these retinal diseases. Several image processing schemes that are considering the retinal vessel segmentation are lacking in segmentation performance and robustness. Laplacian of Gaussian (LoG) detectors is a popular choice method for edge detection adapted for detecting circular blob detection. Laplacian kernel approximates the second-order derivative to the image, which can be effective in combination with Gaussian smoothing in the form of LoG. The LoG detectors are famous for good border detection in noisy images. Based on their parameter, their behavior can be switched between ridge or blob detection. However, their performance generally falls off for elliptical blobs. A generalized LoG detector was proposed recently to deal with elliptical blob detection. Comparing simulation studies for the second-order ridge detector with other popular ridge detectors provides evidence of its effectiveness. The proposed ridge detector shows promise when applied to detect vessels in real-world retinal images of a publicly available database. The method's capabilities are evaluated with a comparison of state of the art, and the performances are obtained on the database most used by researchers. The DRIVE,STARE and CHASE_DB1 databases are used for performance evaluation, and we achieved a sensitivity of **0.785**, a specificity of **0.967** and an accuracy of **0.952** on the DRIVE database,a sensitivity of **0.788**, a specificity of **0.966** and a precision of **0.951** and a sensitivity of **0.787**, a specificity of **0.968** and a precision of **0.952** on CHASE_DB1.

INDEX TERMS Laplacian of Gaussian, ridge detection, blob detection, retinal vessel extraction.

I. INTRODUCTION

Automatic blob detection is considered one of the most important steps to analyze many images. The blob can be a representation of homogeneous regions in the geophysical data [1], the organization of nuclei in the cultivated colony [2], the locations of the tumors in the MRI or CT images [3], [4], recognition hand gesture [5], optical disc [6]–[9], pupil or iris [10]–[14]. A blob is explained as a connection of regions bound at a local extreme, either a maximum for a lighter blob with a darker background or a minimum blob (known as a darker blob) with a darker background [15]. There are many methods of blob detection. Laplacian operator based blob detectors is based on a filter function with large weights related to the central pixels relative to their surrounding region. For manipulation, noise sensitivity, Gaussian smoothing is used first, but such an arrangement results in an operator called Laplacian of Gaussian (LoG) [16]. The loG is becoming a tool for detecting blobs because it allows obtaining a maximum response from the center of the spot as structure [17].

The eccentricity of the blob plays a vital role in detecting the center points because a greater eccentricity of the blob means a greater discrepancy in the detection of the

The associate editor coordinating the review of this manuscript and approving it for publication was Ahmed Mohamed Ahmed Almradi.

This work is licensed under a Creative Commons Attribution 4.0 License. For more information, see https://creativecommons.org/licenses/by/4.0/

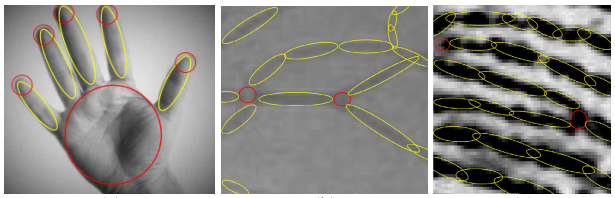

FIGURE 1. Elliptical blob modelling. (a) shows a hand gesture modelled, (b) the retinal vessel modelling, and (c) a fingerprint ridge lines modelled.

centers. In many practical situations like hand and retinal vessel structure, the elliptical blob may occur [18], [19]. The main purpose is to monitor the number of well-defined hand postures to communicate better or track the retinal vessels. But the detection of retinal vessels requires image enhancement, and it contains ridge structure, and it is necessary to achieve appropriate enhancement for retinal vessel segmentation with improved performance, by way of illustration is shown in Fig. 1.

Ridges are considered an important characteristic of image [20], [21]. Ridges have been widely studied in [22], [23] and combustion simulations [24] in the computer vision, in tensor analysis. For segmentation purposes, the ridge's extraction may be divided into three categories [25]. The first refers to the descriptors proposed in [22] for scale-normalized differential geometry. In two-dimensional image space, the differential descriptor produces a one-dimensional ridge curve. However, the descriptors generally capture an extensive object rather than a full cross-section of the object with the major axis of symmetry. In addition, it is severely restricted by the local contrast of the ridge to identify the differential descriptor response [26]. In experimental conditions, we hardly ever have high local contrast for all image regions because of uneven illumination and background noise.

An example of this category is commonly described in the medical image domain [27]–[29]. As proposed in [30], the third category is the tracking of vessels with manual seed. Recent work in [31] has also been reported.

Another exciting way to increase the contrast of an extended object is by turning it in a single binary output. A symbolic thing, approximate by a map with the first-order formulation Taylor, can be considered to constitute a circulatory object around each point in the elongated object. The rule led to a refined form modification technique. A shape adaptation algorithm based on previous works by Lindeberg and Garding [32], is provided by Mikolajczyk and Schmid [33]. This algorithm estimates affinity in two iteratively applied stages: location detection and affinity deformations. An invariant detector based on geometry is initially applied to several isotropic points of interest (location + scale). Then the image passes through several passages of anisotropic smoothness until convergence with an increase in the matrix of the estimated second stage. [34] later shows that the algorithm produces similar results by changing the second-moment matrix to the Hessian one. In contrast with earlier differential ridge measurement, the affine adaptation of ridges and model-based frame detection, the proposed normalized second-order ridge detector is correlated.

On the other hand, if we compare the supervised method with unsupervised, still have their merit in the field. For example, deep learning methods are highly dependent on a training dataset. They always require a large number of images to train a network. Training itself is a time-consuming task that requires a high-end GPU based system [35]. Even a slight variation in the dataset can lead to training on that dataset again. In the case of retinal vessels, mostly the datasets are very small, like for DRIVE comprises only 40 images (20 training and 20 testings) with ground truth. In the case of STARE and CHASE, only 20 and 28 images are available. There isn't any training set available for these two datasets. In such cases, half images are used for training and a half for testing. Training a network on such a small training dataset does not give good results. Augmentation is mostly used to synthetically generate a large dataset from these small datasets for training. Another problem with deep learning-based algorithms is they can't be trained on large image sizes due to hardware constraints. Therefore, traditional methods still have potential in an application where the training dataset is either not available or small in size. The image size is large and in an environment that requires a small number of hardware resources. These reasons motivated authors to work on the traditional method.

The paper is organized as follows. Section II describes the popular ridge detectors and their use for vessel segmentation. In Section III propose method is presented. Experimental results are presented in Section IV and finally the paper is concluded in Section V.

II. POPULAR RIDGE DETECTORS FOR VESSEL SEGMENTATION

This section presents a modified normalized GLoG detector that is used to produce a normalized 2nd-order detector to find ridges, which is an intensity image is another important feature. The second derivative of anisotropic Gaussian (SDAGK) core detection was recently proposed by researchers in [36]. Such kernels, which have demonstrated success in the detection of edges and corners, offer interest. With the detection of a ridge, the increased sensitivity at intersections includes these benefits. This research describes an algorithm that maximizes the size of a Gaussian derivative Filter bank of anisotropic second order, but it does not explicitly deal with a normalization problem of scale. Now the NGLoGs are provided by comparing the definition of SDAGKs:

$$NGLoG\left(x, y; \sigma_x, \sigma_y\right) = \sigma_x^{\alpha}\sigma_y^{\beta}\frac{\partial^2 G(x, y; \sigma_x, \sigma_y)}{\partial x^2} + \sigma_x^{\beta}\sigma_y^{\alpha}\frac{\partial^2 G(x, y; \sigma)}{\partial y^2}. \quad (1)$$

where $\alpha, \beta > 0$, $G(x, y; \sigma)$ is an isotropic Gaussian function, $G(x, y; \sigma_x, \sigma_y)$ is an asymmetric generalized 2D Gaussian function, σ is the standard deviation. For more details about these operators please refer to [37].

It can be observed that the first term of NGLoG can constitute a normalized SDAGK for ridge detection. That is, the normalized second-order derivative of anisotropic Gaussian kernel (NSDAGK) is defined as

$$NSDAGK\left(x, y; \sigma_x, \sigma_y\right) = \sigma_x^{\alpha}\sigma_y^{\beta}\frac{\partial^2 G(x, y; \sigma_x, \sigma_y)}{\partial x^2}. \quad (2)$$

The detection of the computerized vessel is helpful for a set of eye condition named diabetic retinopathy [19], [38], [39]. Diabetic retinopathy is an ongoing disorder and at the early stages, there are no symptoms that it becomes serious [40]. The normal diabetic retinopathy screening leads to a large number of retinal images, which the ophthalmologists must analyze. Since manual testing is expensive, an automated retinal image screening device is the best option [41]–[43]. First, some popular models of the ridge are described and then their performance contrasts with the proposed detector of the ridge. A public DRIVE database is used for evaluation purposes.

A. RIDGE STRENGTH MEASURE

A differential descriptor based on ideal ridge definition was proposed earlier in [22], referred to as ridge strength measure here. The ridge detection strategy first finds scales for each point of the image where normalized ridge measure attains local maxima over scales. Scale map provides locations for the pixels to be picked from the stack of scale-space images to form an enhanced image. The rationale for proposing this ridge measure is the fundamental principle that a ridge is a set of points where the intensity attains a maximum (minimum) value in the main principal direction of the *Hessian* matrix. The underlying assumed ridge model is the *cylindrical ridges* with Gaussian cross-sectional profile. To use measure for retinal vessel extraction, the following procedure is adopted.

Step 1 An acquired retinal image $f(x, y)$ is pre-processed to form a smooth image with uniform background $f_u(x, y)$.

Step 2 Uniform image $f_u(x, y)$ is convolved with a Gaussian function $\frac{1}{2\pi\sigma^2}e^{-\left(x^2+y^2\right)/2\sigma^2}$ with linearly increasing standard deviation σ, to create a stack of scale-space images $f_u(x, y; \sigma)$.

Step 3 While the scale-images $f_u(x, y; \sigma)$ are created, their associated second-order partial derivatives, f_{xx} second-order partial derivative in x direction, f_{yy} second-order partial derivative in y direction and f_{xy} the mixed second-order partial derivatives, are also computed on the way. Discrete derivatives are based on the approximations as described in [22]. The derivatives of the scale images provide us with means to form ridge strength measure for each point (x, y), that is,

$$R_{norm}L\left(x, y, \sigma\right) = \sqrt{\sigma^6 F_x^{+2}\left(F_x^{-2} + 4f_{xy}^2\right)}. \quad (3)$$

where $F_x^{+} = \left(f_{xx} + f_{yy}\right)$ and $F_x^{-} = \left(f_{xx} - f_{yy}\right)$.

Step 4 Next, the $R_{norm}L\left(x, y, \sigma\right)$ is maximized over scales σ to provide scale map $S(x, y)$ for uniform image under consideration. The scale image then provides guidance in choosing corresponding intensities from the normalized differential measure, defined for each scale image, to yield enhanced image $f_{enh}(x, y)$. That is, $S\left(x, y\right) = \max_{\sigma_i<\sigma<\sigma_f} R_{norm}L\left(x, y; \sigma\right)$

Fig. 2(a) depicts the qualitative behavior of the ridge strength measures for retinal vessel image. It can be clearly seen that the measure performs well for extracting the central part of most of the vessel tree structure with some minor setbacks. The measure goes well for vessels that have one of their principal curvatures as zero. However, the result registers a weak response to curved ridges and bifurcation points. Even for some vessels, the ridge strength measures give spurious responses to edges as well. The main advantage of this ridge strength measure is to return an accurate estimate of the width of the vessels across its length. The circles corresponding to scales selected for each vessel point confirms this observation as depicted in Fig. 2(a). This information becomes important when we need to calibrate the vessels to compute their diameters during eye checkups for diabetic retinopathy disease progression.

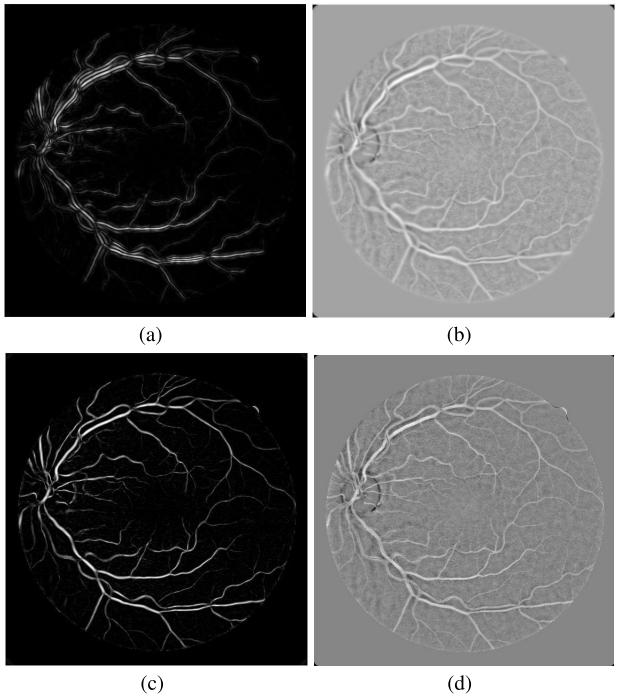

FIGURE 2. Retinal Vessel Enhancement. (a) Lindberg Ridge Measure, (b) Almansa Shape Adaption, (c) Frangi, (d) Proposed.

B. AFFINE SHAPE ADAPTION

Differential descriptors instead of detecting the ridge lines can be more useful if allowed to learn the whole cross-section of the vessel as it travels along the entire length. Thus, the local shape of the vessel can be adapted to create an

enhanced retinal vessel. For this purpose, researchers used the *second-moment matrix* μ to estimate the affine shape of local image regions and then enhance features based on shape adopted. For the case of retinal vessels, the shape will be in the form of an elongated ellipse. The procedure is refined the initial estimate of the second-moment matrix μ iteratively to match local affine shape till it converges. The details are provided in [34]. For the purpose of testing Affine Shape Adaptation for retail vessel extraction, we will follow the same procedure as described in the previous section till Step 3, however, Step 4 will be modified as follows.

Step 4 The $R_{norm}L(x, y; \sigma)$ is maximized over scales to produce a scale image, $S(x, y)$, that is

$$S(x, y) = \arg\max_{\sigma_i < \sigma < \sigma_f} R_{norm}L(x, y; \sigma). \quad (4)$$

The scale image is used to produce a smooth image using correspondence with linear scale-space stack of images. That is,

$$f_s(x, y) = \max_{\sigma_i < \sigma < \sigma_f} f(x, y; , \sigma). \quad (5)$$

Step 5 The smooth image $f_s(x, y)$ is used next to compute second-moment matrix μ as

$$\mu = \begin{bmatrix} f_x^2 & f_x f_y \\ f_x f_y & f_y^2 \end{bmatrix} \quad (6)$$

This leads to forming diffusion matrix $\sum_\sigma = \sigma^2 \frac{\sum}{\|\sum\|}$, where $\sum = \mu^{-1}$, and $\|\sum\|_{\lambda_{\min}}$ represents the minor axis of the ellipse defined by $\sum$.

Step 6 Now our earlier smoothed image $f_s(x, y)$ is smoothed again with this affine-adapted Gaussian Kernel

$$\frac{1}{2\pi \det\left(\sum_t\right)} e^{-\frac{\mathbf{x}^T \sum_t^{-1} x}{2}}$$

, where $\mathbf{x} = (x, y)^T$. This form an updated enhanced image, and a new μ is computed from it. The new updated μ will result in another pass of smoothing previously available smooth image.

Step 7 The process stated in Step 7 is iterated till there is relatively little change in μ matrix, and we get a convergent shape-adapted smoothing for our original image $f_{shape}(x, y)$

The Affine Shape Adaptation works better as compared to the ridge strength measure as it provides better contrast for the whole length and breadth of the vessel rather than just tracking the centerline. However, relating classical differential geometry concepts with discrete differential geometry has its own limiting issues. The shape adaptation takes place inclemently and can be hindered at any slight perturbation, which will cause object shape distortion for the underlying true vessel segment. To provide numerical stability, regularization constraint is employed that limits its smoothness power, as evident in affine shape adaptation for fingerprint images in [44]. The Fig. 2(b) depicts the result of affine shape adaptation result for the input retinal image; what we observe is that vessels emerge with homogeneous and high intensity across their entire length, but edges are blurred. The result lacks adequate suppression capability of the background noise.

C. FRANGI VESSELNESS MEASURE

Frangi *et al.* [45] proposed a vessel measure with its own Hessian matrix values, which effectively separates the linear structure from structures like a blob and plate-like structures and suppresses random background noise. The vessel measurement in nature is multidimensional to suit various vessel sizes. A Frangi's [45] vessel filter is implemented to measure its ability to detect vessels in retinal images. The method is described as follows.

Step 1 The acquired image $f(x, y)$ is converted to a smooth uniform image with improved contrast, as done earlier, into $f_u(x, y)$.

Step 2 The Hessian matrix in the point (x, y) at scale σ, $H(x, y; \sigma)$,is computed using Gaussian derivatives:

$$H(x, y; \sigma) = \begin{bmatrix} f_{xx} & f_{xy} \\ f_{xy} & f_{yy} \end{bmatrix}, \quad (7)$$

where f_{xx}, f_{yy}, and f_{xy} are partial second-order derivative computed at scale images corresponding to scale σ.

Step 3 The decomposition of the local Hessian matrix for each poingt of the image extracts the eigenvalues ($|\lambda_1| \leq |\lambda_2| \leq |\lambda_3|$) and principal direction ($\bar{u}_1, \bar{u}_2, \bar{u}_3$). An ideal tubular structure implies $|\lambda_1| \approx 0, |\lambda_1| \ll |\lambda_2|, \lambda_2 \approx \lambda_3$, with $\bar{u}_1$ the direction of minimal curvature (along the vessel).

Step 4 Using this information, vesselness measure V_F^σ is designed to measure the similarity of a given structure to an ideal Gaussian profile as:

$$V_F^\sigma = \begin{cases} 0 & if\ \lambda_2 > 0\ or\ \lambda_3 > 0 \\ \left(1 - \exp\left(-\frac{R_A^2}{2\alpha^2}\right)\right) \exp\left(-\frac{R_B^2}{2\beta^2}\right) & \\ \left(1 - \exp\left(-\frac{S^2}{2c^2}\right)\right) & \end{cases} \quad (8)$$

where the sensitivity of a filter to dissimilarity measures between the tube-like and plate-like structures are regulated by using α, β, cR_A, blob-like R_B and background (S):

$$R_A = \frac{|\lambda_2|}{|\lambda_3|} \quad (9)$$

$$R_B = \frac{|\lambda_1|}{|\lambda_2 \lambda_3|} \quad (10)$$

$$S = \sqrt{\lambda_1^2 + \lambda_2^2 + \lambda_3^2} \quad (11)$$

Step 5 The final measurement integrates filter responses at various scales with the maximal response:

$$V_F^{\sigma}(x) = \max_{\sigma_{\min} \le \sigma \le \sigma_{\max}} V_F^{\sigma}(x) \tag{12}$$

We can analyze from the result of retinal vessel enhancement in Fig. 5(c) that complete vessel cross-section is enhanced with excellent nice suppression of the background. However, the response of the vesselness measure is not uniform across the whole length of the vessel tree, some segments remain dark. This is primarily due to the setting of the parameters (α, β, c) values used in the vesselness measure, which may work in one region of the image while may not be useful in another region. The second issue is that the model was developed specifically for tubular structures having Gaussian cross-sectional profile. Therefore wherever the vessels shape to deviate from Gaussian cross-sectional profile such as at the bifurcation or junction points, the vesselness measure does not provide adequate response [46].

III. PROPOSED METHOD

The article is about comparing the existing edge enhancement methods to develop an improved detector. The theory for the proposed method sort of evolves from the other methods explained in previous sections.

A. PRE-PROCESSING MODULE

The image quality of all datasets is not good enough for using it directly with ridge detector. The images possess a varied contrast and noisy areas. It is an important step to smooth the image first and then passing it to a detector for better performance.

A series of pre-processing steps are carried out to prepare the retinal image for final detection with computerized ridge models. These are enumerated as follows:

1) In the first task, the color image (red, green, and blue channels) is converted into a single channel grayscale image. Instead of picking a green channel for its possible gray-scale representation, Principal Component Analysis (PCA) is employed to achieve gray-scale conversion. First, a vectored color image ($f_{rgb} \in \mathbb{R}^3$ is created. Then, a zero-mean YCbCr image ($f_{ycc} \in \mathbb{R}^3$) is computed. For this purposed, the conventional transfer function $f(\cdot)$ operation is used to separate luminance and chrominance channels. The transfer function is as follows:

$$\begin{aligned} Y &= (0.257 * R) + (0.504 * G) + (0.098 * B) + 16 \\ Cr &= (0.439 * R) - (0.368 * G) - (0.071 * B) + 128 \\ Cb &= -(0.148 * R) - (0.291 * G) + (0.439 * B) + 128 \end{aligned}$$

where luminance channel is Y and chrominance channels are Cb and Cr.
Next, three eigenvalues $(\lambda_1 \ge \lambda_2 \ge \lambda_3 \in R^1)$ and corresponding normalized eigenvectors $(v_1, v_2, v_3 \in R^2)$ are obtained by PCA. The resultant gray image $(f_{gray} \in \mathbb{R}^2)$, is computed by weighted linear combination of three projections, where weighted as computed by their eigenvalues. The output at the end is scaled to [0, 255]. Note that for the projection outcomes in the corresponding vectors, we use eigenvalues values as weighting factors. As a consequence, the first subspace projection dominates color-to-gray mapping and the second and third subspace projections are retaining the grey image information. Fig. 3 shows the entire conversion process for an input color image by demonstrating the images resulting. The histogram in the figures 4(b) of $fgry$ is more distributed than in the figures 4(a) of fg, which means that the proposed transformation method is effectively mappable.

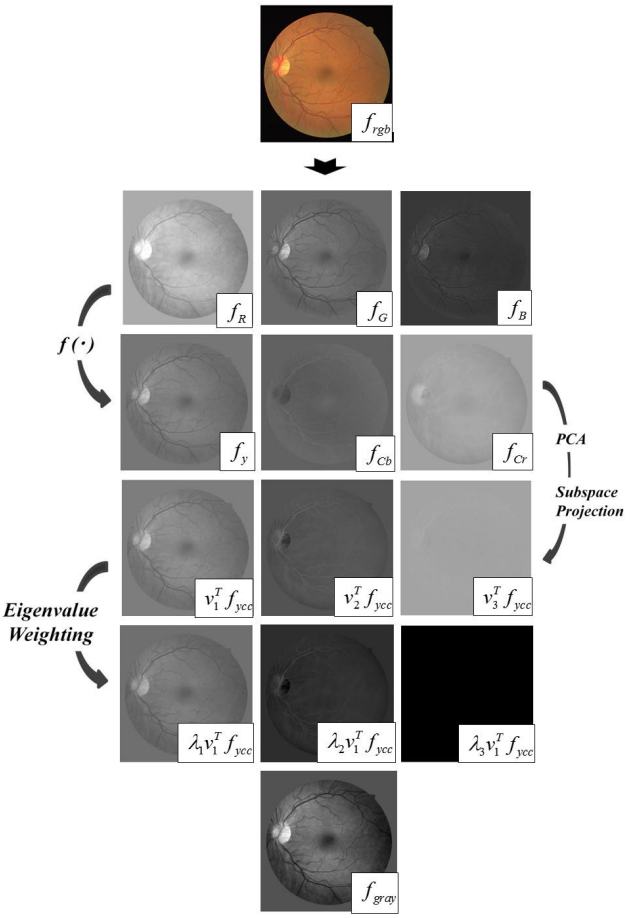

FIGURE 3. PCA-based color-to-gray image conversion.

2) For compensating the variation in brightness a subtraction method is employed here. A background image f_B is produced by applying a large 21×21 median filter, which is constructed of twice the width of largest vessel width present in the image, resulting in the square kernel. Increasing filter size can give similar result but it will add more computational complexity. Smaller size can may not be able to remove some larger vessel. Therefore, 21×21 filter size found to be an optimal size for DRIVE and STARE datasets. Then, the difference

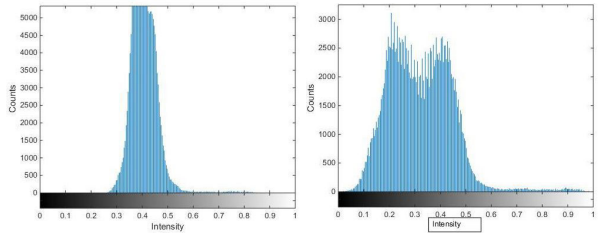

(a) (b)

FIGURE 4. (a) Histogram of green channel f_G, (b) Histogram of PCA-based grayscale image$f_{Gray}(x, y)$.

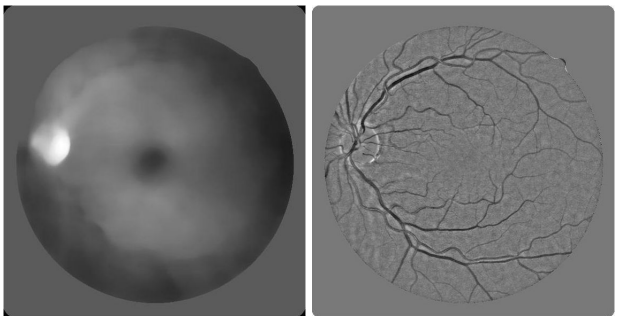

(a) (b)

FIGURE 5. (a) Background image, (b) Background subtracted image.

f_D between the image f and the background estimation image f_B is calculated pixelwise as

$$f_D(x, y) = f(x, y) - f_B(x, y) \tag{13}$$

The subtraction results in low contrast for the difference image. The difference image f_D is then linearly stretched to cover the whole allowable dynamic range. This results in an image with better local contrast and uniform background image $f_u(x, y)$.

The PCA transformation changes linearly correlated three color bands (Red, Green, and Blue) into uncorrelated bands (Y, Cb, and Cr). In the transformation process, we need to remove the DC Mean image (average of all three color images) first. The specific reason is that it only represents average brightness but no useful discriminating features. The large DC average values removal from images is called zero-mean standardization. It is necessary to emphasize relatively small valuable features present in these images. If not done so, then the average value will dominate the variance maximization process that will create undue bias.

B. PROPOSED DETECTOR

The novelty of this work relies on introducing an improved edge operator with the name normalized Gaussian Derivative Kernel (NSAGDK) in the second order. The operator is anisotropic that adopts an underlying elongated feature. Furthermore, its normalizing constants are expressed in terms of length and width parameters. They are placed in the front to provide an equal response across all scales. The presence of these normalizing constants is essential to getting optimal response even for fine vessels. Picking fine and large vessels with ease is the novelty of the proposed operator.

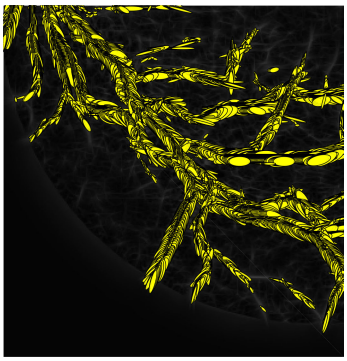

FIGURE 6. Shifted, rotated Elliptical blob representation for retinal vessels.

The overlapping use of the elliptical blobs is used to cover long vessels, as shown in Fig. 6. This shows that vessel detection can be done with NGLoG. However, if we keep the first term of the NGLoG expression, we can identify a better alternative, leading to the normalized Gaussian Derivative Kernel (NSAGDK) in the second order. With the retinal image, the normalized SAGDK is used as follows:

Step 1 As explained in the pre-processing section of the module, the input image $f(x, y)$ is transmitted through several pre-processing steps to create a consistent smooth $f_u(x, y)$ image.

Step 2 A uniform image $f_u(x, y)$ is passed through a normalised SAGDK filter bank of thickness $\sigma_x = (0.5, 1, 1.5, 2)$ and length $\sigma_y = (5, 7, 9, \ldots, 21)$ pixel units. In addition, the detector template for a specific choice of σ_x and σ_y is rotated to match the directional image orientation θ. Therefore, we have $NSAGDK(R_\theta \mathbf{x})$, where R_θ is the rotation matrix $\begin{pmatrix} \cos\theta & \sin\theta \\ -\sin\theta & \cos\theta \end{pmatrix}$ to align detector with vessel direction of the directional image. With application of this aligned normalised SDAGK detector for a specific choice of σ_x, σ_y, we get $f_N(x, y; \sigma_x, \sigma_y)$.

Step 3 The normalized images can be combined with the σ_x and σ_y values as a single enhanced image. Therefore, we have

$$f_{enh}(x, y) = \max_{\substack{\sigma_{x,i} \le \sigma_x \le \sigma_{x,f} \\ \sigma_{r,i} \le \sigma_y \le \sigma_{y,f}}} f_N\left(x, y; \sigma_x, \sigma_y\right). \tag{14}$$

The Equation 14 shows that the proposed operator value at any given location is the maximum of all responses computed by assigning a set of values to σ_x and σ_y. One parameter is related to the length of the feature. The other one is the width of the feature under investigation. A max operator's presence in the proposed technique's definition is responsible for avoiding fusing fine vessels. Furthermore, the set of values associated with parameters σ_x and σ_y, contains small enough values to pick fine vessels, which are generally speaking of shorter length and width. This arrangement makes utmost care at not smoothing edges. A bilinear interpolation is used to cover interruptions caused by pixels lying between integer

TABLE 1. Performance analysis of proposed method with existing popular ridge detectors on DRIVE database.

	Sensitivity		Specificity		Accuracy	
	Average	Std devi.	**Average**	Std devi.	**Average**	Std devi.
Ridge Strength Measure	**0.7487**	0.0652	**0.9509**	0.0662	**0.9253**	0.0667
Affine Shape Adaption	**0.7401**	0.0640	**0.9532**	0.0666	**0.9263**	0.0663
Frangi Vesselness Measure	**0.7520**	0.0651	**0.9528**	0.0598	**0.9283**	0.0556
Proposed	**0.7855**	0.0621	**0.9678**	0.0538	**0.9523**	0.0556

TABLE 2. Performance analysis of proposed method with existing popular ridge detectors on STARE database.

	Sensitivity		Specificity		Accuracy	
	Average	Std devi.	**Average**	Std devi.	**Average**	Std devi.
Ridge Strength Measure	**0.7311**	0.0678	**0.9392**	0.0675	**0.9235**	0.0509
Affine Shape Adaption	**0.7221**	0.0532	**0.9350**	0.0676	**0.9210**	0.0602
Frangi Vesselness Measure	**0.7289**	0.0592	**0.9393**	0.0563	**0.9301**	0.0621
Proposed	**0.7881**	0.0592	**0.9666**	0.0563	**0.9512**	0.0621

coordinates for affine transformation. Due to the presence of optimal normalization weights, the proposed method is able to pick fine small features of interest.

The noisy pixels are avoided by providing an appropriate set of values for length and width parameters of the proposed operator. The set contains values that start at a minimum and goes up to a maximum value. The minimum value in the set is chosen large enough to avoid noisy pixels. The essence of the technique is in introducing normalization constants in terms of length and width parameters. The proposed scheme employs normalization constants $\sigma_x^{\alpha}\ \sigma_y^{\beta}$, with optimal values of α and β as 1.5 and 0.5, respectively.

The output result of NSAGDK displayed in Fig. 5(d) shows that vessels are accentuated compared to their background. The junctions and bifurcation points are well-preserved. However, its background noise suppression is not adequate. Therefore, it may be suggested to combine the NSAGDK function with the noise suppression term of the vesselness measure to provide a better signal-to-noise performance. This is the focus of our on-going research work.

IV. EXPERIMENTAL RESULTS

A. DATABASE AND PARAMETERS

Three publicly available DRIVE [47],[1] STARE [48][2] and CHASE_DB1 [53][3] databases are mainly used for experimental purposes.

The DRIVE database contained 40 retinal fundus images of different levels of disease progression. The 3CCD camera is used to collect these images, and the anatomical structure includes the central circular area with a radius of approximately 540 pixels. The database is divided into two groups of images: the training images set and the testing images set. Each set contains 20 images taken on different patients. Each image in the two sets includes a manual segmentation of retinal blood vessel images known as the reference image or good standard image.

The STARE database contains 20 retinal fundus images with their corresponding mask images and ground truth images. These images are captured using the Topcon TRV-50 background camera. These images have a resolution of 650 pixels, and 50 % of the images in the STARE database contain ten pathologies images. Performance evaluation of retinal blood vessel segmentation methods on the STARE database is challenging.

Child Heart And health Study in England (CHASE_DB1) comprises of total 28 images that are acquired from both eyes of 14 multiethnic children in England. Each image consists of a high resolution of 999 × 960 pixels.

In this research, the sensitivity (*Se*), specificity, and accuracy (*Sp*) were evaluated in our algorithm. *Se* and *Sp* give the best vessel and non-vessel information. *Acc* provides overall pixel information, the mathematical measurement of the following parameters:

$$Sensitivity = \frac{TP}{TP + FN}. \tag{15}$$

$$Specificity = \frac{TN}{TN + FP}. \tag{16}$$

$$Accuracy = \frac{TP + TN}{TP + FP + FN + TN}. \tag{17}$$

B. PERFORMANCE COMPARISON ON RIDGE DETECTION METHODS

First, as shown in Table 1 and Table 2, the proposed method performance is assessed with average accuracy, sensitivity,

[1]The dataset is widely available at https://drive.grand-challenge.org/

[2]More information regarding the STARE project can be found at https://cecas.clemson.edu/~ahoover/stare/

[3]The dataset can found at https://blogs.kingston.ac.uk/retinal/chasedb1/

TABLE 3. Comparison with state-of-the-art techniques on the CHASE_DB1 database.

Type	Methods	Year	Sn	Sp	Acc	AUC
Supervised methods	Alom [49]	2018	0.7756	0.9820	0.9634	0.9815
	Yan [50]	2018	0.7633	0.9809	0.9610	0.9781
	Oliveira [51]	2018	0.7779	0.9864	0.9653	0.9855
	Jiang [52]	2019	0.7839	0.9894	0.9721	0.9866
Unsupervised methods	Zhang [53]	2016	0.7626	0.9661	0.9452	0.9606
	Karn [54]	2018	0.78	0.97	0.97	N.A
	Proposed	2021	0.7875	0.9682	0.9521	N.A

TABLE 4. Comparison of Proposed Method with published Methods.

	Sensitivity		Specificity		Accuracy	
	Average	Std devi.	**Average**	Std devi.	**Average**	Std devi.
Human observer [55]	**0.7761**	0.0593	**0.9725**	0.0082	**0.9473**	0.0048
Chaudhuri [56]	**0.2716**	0.2118	**0.9794**	0.0388	**0.8894**	0.0321
Jiang [57]	**0.6478**	0.0642	**0.9625**	0.029	**0.9222**	0.0069
Zana [58]	**0.6696**	0.0764	**0.9769**	0.0079	**0.9377**	0.0077
Perez [59]	**0.7086**	0.1815	**0.9496**	0.0260	**0.9181**	0.239
Azzopardi Symmetric [60]	**0.7526**	0.0622	**0.9707**	0.0092	**0.9427**	0.0780
Azzopardi Asymmetric [60]	**0.7499**	0.0522	**0.9621**	0.0192	**0.9422**	0.0710
Proposed	**0.7855**	0.0651	**0.9678**	0.0598	**0.9523**	0.0556

and specificity. However, the sensitivity of this method is better on the DRIVE database than other ridge detection methods and some state-of-the-art methods. Also, the accuracy is a little higher than other ridge detection methods. This shows that we can detect smaller blood vessels with our method.

The performance of our approach is also analyzed, as presented in table 1 and table 2, using existing famous DRIVE and STARE databases. We improved the accuracy and sensitivity than other methods.

Table 4 compares the method performance with methods that have recently been implemented in the DRIVE database, which include standard deviations. More importantly, the sensitivity, specificity, and accuracy of the human observer are shown in Table 4 by using manual segmenting data from the second observer. The sensitivity of the proposed method is, $Se = 0.7610$, higher than all supervised methods presented in Table 4. The proposed method gives slightly better accuracy than both Azzopardi Symmetric [60] and Azzopardi Asymmetric [60] while its specificity is somewhat lower than both Azzopardi Symmetric [60] and Azzopardi Asymmetric [60]. Overall, the proposed method provides better performance than almost all existing methods, particularly the sensitivity.

On CHASE_DB1 dataset, the proposed method performed better than the existing techniques as reported in Table 3.

C. ANALYSIS OF TINY VESSELS

Numerous segmentation methods are implemented, but limitations have been observed in all methods, and there is a lack of small vessels detection and decreased sensitivity. These two limitations are related to each other because the correct detection of small vessels improved the sensitivity of the retinal vessel detection methods. We focused on the detection of tiny vessels. For the observation, we compare the result of the proposed method with the best-known methods (Nguyen *et al.* [55] and Zhao *et al.* [61]) based on the detection of small vessels, and our method gave improved sensitivity as shown in the Table 4.

D. PERFORMANCE ANALYSIS ON CHALLENGING RETINAL IMAGES

The ability of retinal vessels segmentation method can be tested on difficult images, and challenging images mean that the images contain pathologies. Our proposed method has the capabilities to detect appropriate vessels from challenging images. Figure 14 shows the comparison of the results of our method on challenging images compared to the Hou [73], and Nuygen [55] methods. We observe that tiny vessels are dropped in the Hou's and Nuygen's methods.

E. COMPARATIVE ANALYSIS ON SUPERVISED AND UNSUPERVISED METHODS

The method's ability to accurately segment vessels is proven by comparing the performance of the proposed methods with existing methods. The two most widely available public databases are used, called DRIVE and STARE, for evaluation purposes in almost all methods. Table 5 shows the comparison of the performances of our proposed method with the existing methods, and our proposed method gives comparable performances with the existing methods.

TABLE 5. Performance Analysis of Segmentation Model.

		DRIVE				STARE			
Methods	Year	Se	Sp	AC	AUC	Se	Sp	AC	AUC
Zhao et al [61]	2016	0.716	0.978	0.944	0.848	0.776	0.954	0.943	0.865
Melinscak et al [62]	2016	-	-	0.946	0.974	-	-	-	-
Soomro et al [63]	2016	0.714	0.968	0.946	-	0.709	0.965	0.942	-
Khan et al [64]	2016	0.737	0.967	0.951	-	0.736	0.971	0.951	-
Soomro et al [65]	2017	0.752	0.976	0.943	0.969	0.784	0.981	0.961	0.981
Soomro et al [66]	2017	0.746	0.966	0.952	-	0.755	0.959	0.951	-
Soomro et al [67]	2017	0.746	0.917	0.948	0.831	0.748	0.922	0.947	0.835
Soomro et al [68]	2018	0.752	0.976	0.953	-	0.786	0.982	0.967	-
Soomro et al [69]	2018	0.739	0.956	0.948	0.844	0.748	0.962	0.947	0.855
Khan et al [70]	2018	0.769	0.965	0.950	-	0.752	0.981	0.951	-
Soomro et al [71]	2019	0.745	0.962	0.948	-	0.784	0.976	0.951	-
Soomro et al [72]	2019	0.802	0.974	0.959	0.948	0.801	0.969	0.961	0.945
Proposed Method	2020	0.785	0.967	0.952	0.956	0.788	0.966	0.951	0.947

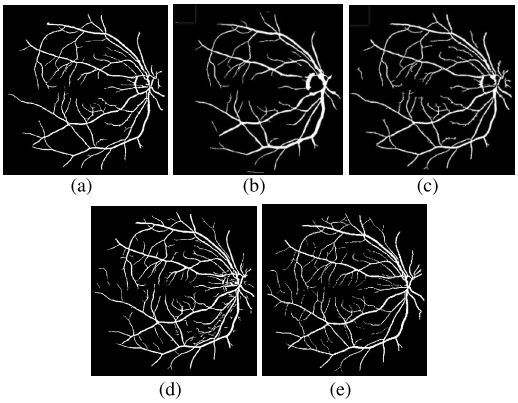

FIGURE 7. Consider that Figure (e) shows the result of our proposed segmentation method, and which is compared to the output of Nguyen *et al.* [55] (as shown in Figure (a)), and Zhao *et al.* [61] (as shown in Figure (b) and Figure (c)) with the image of the gold standard (as shown in Figure (d)).

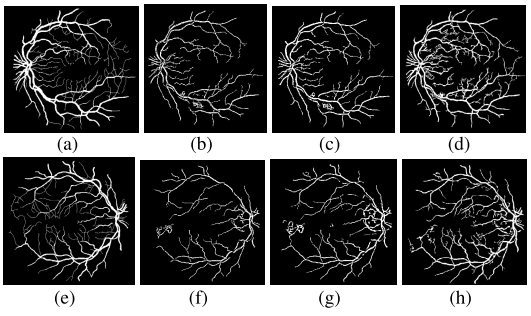

FIGURE 8. The capabilities of the proposed retinal vessel segmentation method are tested on pathology images. Figure (a) and Figure (e) are manually segmented images. Figure (d) and Figure (h) are shown the segmented output images of our proposed method as a comparison of the output images of Nuygen (shown in Figure (b) and Figure (f)) and Hou (as shown in Figure (c) and Figure (g)).

V. CONCLUSION

Variations in retinal blood vessel diameters can be used as a tool for diagnosing eye diseases. For eye disease diagnosis, the accurate detection of vessels is an essential task. Accurate segmentation of retinal vessels in the presence of pathologies and noise is a difficult task. In the literature, many ways of retinal blood vessel segmentation are suggested. The generalized LoG function has shown the capability to model objects in some interesting imaging applications. We can use this behavior as a blob detector or as the ridge detector by setting the parameter to σ. In this paper, the generalized LoG function is used as a ridge detector and is compared with some famous ridge detectors. For experiments, some famous ridge detectors are implemented, and their performance is observed on retinal images. It is observed that the proposed GLoG function, when used as a ridge detector, much gives better performance as compared to the other existing ridge detectors. The proposed method was evaluated on the DRIVE,STARE and database to observe the impact of our method compared to other existing methods for detecting retinal vessels. Our method obtained **0.785**, a specificity of **0.967** and a accuracy of **0.952** on the DRIVE database and a sensitivity of **0.788**, a specificity of **0.966** and a accuracy of **0.951** and on CHASE_DB1, we achieved a sensitivity of **0.787**, a specificity of **0.968** and a accuracy of **0.952**. Our method surpasses many existing methods and gives a comparable performance with few methods, and its performance shows that our method can detect precise retinal vessels.

REFERENCES

[1] A. Kaspers, "Blob detection," M.S. thesis, Dept. Med., Utrecht Univ. Repository, Utrecht, The Netherlands, 2011.
[2] Q. Yang and B. Parvin, "CHEF: Convex hull of elliptic features for 3D blob detection," in *Proc. Object Recognit. Supported User Interact. Service Robots*, vol. 2, 2002, pp. 282–285.
[3] T. Logeswari and M. Karnan, "An improved implementation of brain tumor detection using soft computing," in *Proc. 2nd Int. Conf. Commun. Softw. Netw.*, 2010, pp. 147–151.
[4] Z. U. Rehman, S. S. Naqvi, T. M. Khan, M. A. Khan, and T. Bashir, "Fully automated multi-parametric brain tumour segmentation using superpixel based classification," *Expert Syst. Appl.*, vol. 118, pp. 598–613, Mar. 2019.
[5] R. Cipolla, S. Battiato, and G. M. Farinella, Eds., *Computer Vision: Detection, Recognition and Reconstruction*. Cham, Switzerland: Springer, 2010.
[6] Z. U. Rehman, S. S. Naqvi, T. M. Khan, M. Arsalan, M. A. Khan, and M. A. Khalil, "Multi-parametric optic disc segmentation using superpixel based feature classification," *Expert Syst. Appl.*, vol. 120, pp. 461–473, Apr. 2019.

[7] S. S. Naqvi, N. Fatima, T. M. Khan, Z. U. Rehman, and M. A. Khan, "Automatic optic disk detection and segmentation by variational active contour estimation in retinal fundus images," *Signal, Image Video Process.*, vol. 13, no. 6, pp. 1191–1198, Sep. 2019.

[8] M. Tabassum, T. M. Khan, M. Arsalan, S. S. Naqvi, M. Ahmed, H. A. Madni, and J. Mirza, "CDED-net: Joint segmentation of optic disc and optic cup for glaucoma screening," *IEEE Access*, vol. 8, pp. 102733–102747, 2020.

[9] F. Abdullah, R. Imtiaz, H. A. Madni, H. A. Khan, T. M. Khan, M. A. U. Khan, and S. S. Naqvi, "A review on glaucoma disease detection using computerized techniques," *IEEE Access*, vol. 9, pp. 37311–37333, 2021.

[10] M. T. Ibrahim, T. M. Khan, S. A. Khan, M. A. Khan, and L. Guan, "Iris localization using local histogram and other image statistics," *Opt. Lasers Eng.*, vol. 50, no. 5, pp. 645–654, May 2012.

[11] T. M. Khan, M. Aurangzeb Khan, S. A. Malik, S. A. Khan, T. Bashir, and A. H. Dar, "Automatic localization of pupil using eccentricity and iris using gradient based method," *Opt. Lasers Eng.*, vol. 49, no. 2, pp. 177–187, Feb. 2011.

[12] M. T. Ibrahim, T. M. Khan, M. A. Khan, and L. Guan, "A novel and efficient feedback method for pupil and iris localization," in *Proc. Int. Conf. Image Anal. Recognit.* Berlin, Germany: Springer, 2010, pp. 79–88.

[13] T. M. Khan, D. G. Bailey, M. A. Khan, and Y. Kong, "Real-time iris segmentation and its implementation on FPGA," *J. Real-Time Image Process.*, vol. 17, pp. 1–14, Feb. 2019.

[14] T. M. Khan, "Fusion of fingerprint and iris recognition for embedded multimodal biometric system," School Eng., Macquarie Univ., Sydney, NSW, Australia, 2016. [Online]. Available: http://hdl.handle.net/1959.14/1253981

[15] T. Lindeberg, "Feature detection with automatic scale selection," *Int. J. Comput. Vis.*, vol. 30, no. 2, pp. 77–116, 1998.

[16] R. M. Abbas, T. M. Khan, M. A. U. Khan, and H. A. Khan, "Fast and accurate iris segmentation methods using LoG filters," in *Proc. Int. Conf. Comput., Electron. Commun. Eng. (iCCECE)*, Aug. 2019, pp. 124–129.

[17] D. Blostein and N. Ahuja, "A multiscale region detector," *Comput. Vis., Graph., Image Process.*, vol. 45, no. 1, pp. 22–41, Jan. 1989.

[18] L. Bretzner, I. Laptev, and T. Lindeberg, "Hand gesture recognition using multi-scale colour features, hierarchical models and particle filtering," in *Proc. 5th IEEE Int. Conf. Autom. Face Gesture Recognit.*, 2002, pp. 423–428.

[19] T. A. Soomro, J. Gao, T. M. Khan, A. F. M. Hani, M. A. U. Khan, and M. Paul, "Computerised approaches for the detection of diabetic retinopathy using retinal fundus images: A survey," *J. Pattern Anal. Appl.*, vol. 20, no. 4, pp. 927–961, 2017.

[20] M. A. U. Khan, T. M. Khan, T. A. Soomro, N. Mir, and J. Gao, "Boosting sensitivity of a retinal vessel segmentation algorithm," *Pattern Anal. Appl.*, vol. 22, pp. 583–599, May 2019.

[21] A. Khawaja, T. M. Khan, K. Naveed, S. S. Naqvi, N. U. Rehman, and S. J. Nawaz, "An improved retinal vessel segmentation framework using frangi filter coupled with the probabilistic patch based denoiser," *IEEE Access*, vol. 7, pp. 164344–164361, 2019.

[22] T. Lindeberg, "Edge detection and ridge detection with automatic scale selection," *Int. J. Comput. Vis.*, vol. 30, pp. 117–156, Nov. 1998.

[23] T. Schultz, H. Theisel, and H.-P. Seidel, "Crease surfaces: From theory to extraction and application to diffusion tensor MRI," *IEEE Trans. Vis. Comput. Graphics*, vol. 16, no. 1, pp. 109–119, Jan. 2010.

[24] J. H. Frank and S. A. Kaiser, "High-resolution imaging of dissipative structures in a turbulent jet flame with laser Rayleigh scattering," *Experim. Fluids*, vol. 44, no. 2, pp. 221–233, Feb. 2008.

[25] C. Kirbas and F. Quek, "A review of vessel extraction techniques and algorithms," *ACM Comput. Surveys*, vol. 36, no. 2, pp. 81–121, Jun. 2004.

[26] K. Naveed, F. Abdullah, H. A. Madni, M. A. U. Khan, T. M. Khan, and S. S. Naqvi, "Towards automated eye diagnosis: An improved retinal vessel segmentation framework using ensemble block matching 3D filter," *Diagnostics*, vol. 11, no. 1, p. 114, Jan. 2021.

[27] T. M. Khan, A. Robles-Kelly, and S. S. Naqvi, "A semantically flexible feature fusion network for retinal vessel segmentation," in *Proc. Int. Conf. Neural Inf. Process.* Cham, Switzerland: Springer, 2020, pp. 159–167.

[28] T. M. Khan, S. S. Robles-Kelly, A. A. Naqvi, and M. Arsalan, "Residual multiscale full convolutional network (RM-FCN) for high resolution semantic segmentation of retinal vasculature," in *Proc. S+SSPR*. Cham, Switzerland: Springer, 2020, pp. 1–10.

[29] I. Razzak, G. Shoukat, S. Naz, and T. M. Khan, "Skin lesion analysis toward accurate detection of melanoma using multistage fully connected residual network," in *Proc. Int. Joint Conf. Neural Netw. (IJCNN)*, Jul. 2020, pp. 1–8.

[30] E. Bekkers, R. Duits, T. Berendschot, and B. ter Haar Romeny, "A multi-orientation analysis approach to retinal vessel tracking," *J. Math. Imag. Vis.*, vol. 49, no. 3, pp. 583–610, Jul. 2014.

[31] U. Sharma and R. Duits, "Left-invariant evolutions of wavelet transforms on the similitude group," *Appl. Comput. Harmon. Anal.*, vol. 39, no. 1, pp. 110–137, Jul. 2015.

[32] T. Lindeberg and J. Gårding, "Shape-adapted smoothing in estimation of 3-D shape cues from affine deformations of local 2-D brightness structure," *Image Vis. Comput.*, vol. 15, no. 6, pp. 415–434, Jun. 1997.

[33] K. Mikolajczyk and K. Mikolajczyk, "Scale & affine invariant interest point detectors," *Int. J. Comput. Vis.*, vol. 60, no. 1, pp. 63–86, Oct. 2004.

[34] R. Lakemond, C. Fookes, and S. Sridharan, "Affine adaptation of local image features using the hessian matrix," in *Proc. 6th IEEE Int. Conf. Adv. Video Signal Based Surveill.*, Sep. 2009, pp. 496–501.

[35] T. M. Khan and A. Robles-Kelly, "Machine learning: Quantum vs classical," *IEEE Access*, vol. 8, pp. 219275–219294, 2020.

[36] C. Lopez-Molina, G. Vidal-Diez de Ulzurrun, J. M. Baetens, J. Van den Bulcke, and B. De Baets, "Unsupervised ridge detection using second order anisotropic Gaussian kernels," *Signal Process.*, vol. 116, pp. 55–67, Nov. 2015.

[37] M. A. U. Khan, T. M. Khan, D. G. Bailey, and O. Kittaneh, "Deriving scale normalisation factors for a GLoG detector," *IET Image Process.*, vol. 12, no. 9, pp. 1673–1682, Sep. 2018.

[38] T. M. Khan, F. Abdullah, S. S. Naqvi, M. Arsalan, and M. A. Khan, "Shallow vessel segmentation network for automatic retinal vessel segmentation," in *Proc. Int. Joint Conf. Neural Netw. (IJCNN)*, Jul. 2020, pp. 1–7.

[39] T. M. Khan, S. S. Naqvi, M. Arsalan, M. A. Khan, H. A. Khan, and A. Haider, "Exploiting residual edge information in deep fully convolutional neural networks for retinal vessel segmentation," in *Proc. Int. Joint Conf. Neural Netw. (IJCNN)*, Jul. 2020, pp. 1–8.

[40] M. A. U. Khan, T. M. Khan, S. S. Naqvi, and M. Aurangzeb Khan, "GGM classifier with multi-scale line detectors for retinal vessel segmentation," *Signal, Image Video Process.*, vol. 13, no. 8, pp. 1667–1675, Nov. 2019.

[41] T. A. Soomro, J. Gao, M. A. U. Khan, T. M. Khan, and M. Paul, "Role of image contrast enhancement technique for ophthalmologist as diagnostic tool for diabetic retinopathy," in *Proc. Int. Conf. Digit. Image Comput., Techn. Appl. (DICTA)*, Gold Coast, QLD, Australia, Nov. 2016, pp. 1–8.

[42] M. A. U. Khan, T. M. Khan, K. I. Aziz, S. S. Ahmad, N. Mir, and E. Elbakush, "The use of Fourier phase symmetry for thin vessel detection in retinal fundus images," in *Proc. IEEE Int. Symp. Signal Process. Inf. Technol. (ISSPIT)*, Dec. 2019, pp. 1–6.

[43] A. Khawaja, T. M. Khan, M. A. U. Khan, and S. J. Nawaz, "A multi-scale directional line detector for retinal vessel segmentation," *Sensors*, vol. 19, no. 22, p. 4949, Nov. 2019.

[44] A. Almansa, "Fingerprint enhancement by shape adaptation of scale-space operators with automatic scale selection," Ph.D. dissertation, Comput. Vis. Active Perception Lab., Dept. Numer. Anal. Comput. Sci., KTH Stockholm, Stockholm, Sweden, 1998.

[45] A. F. Frangi, W. J. Niessen, R. M. Hoogeveen, T. van Walsum, and M. A. Viergever, "Model-based quantitation of 3-D magnetic resonance angiographic images," *IEEE Trans. Med. Imag.*, vol. 18, no. 10, pp. 946–956, Oct. 1999.

[46] M. Rudzki, "Vessel detection method based on eigenvalues of the Hessian matrix and its applicability to airway tree segmentation," in *Proc. 11th Int. PhD Workshop OWD*. Gliwice, Poland: Silesian Univ. Technology, 2009.

[47] J. Staal, M. D. Abramoff, M. Niemeijer, M. A. Viergever, and B. van Ginneken, "Ridge-based vessel segmentation in color images of the retina," *IEEE Trans. Med. Imag.*, vol. 23, no. 4, pp. 501–509, Apr. 2004.

[48] A. D. Hoover, V. Kouznetsova, and M. Goldbaum, "Locating blood vessels in retinal images by piecewise threshold probing of a matched filter response," *IEEE Trans. Med. Imag.*, vol. 19, no. 3, pp. 203–210, Mar. 2000.

[49] M. Zahangir Alom, M. Hasan, C. Yakopcic, T. M. Taha, and V. K. Asari, "Recurrent residual convolutional neural network based on U-net (R2U-Net) for medical image segmentation," 2018, *arXiv:1802.06955*. [Online]. Available: http://arxiv.org/abs/1802.06955

[50] Z. Yan, X. Yang, and K.-T. Cheng, "Joint segment-level and pixel-wise losses for deep learning based retinal vessel segmentation," *IEEE Trans. Biomed. Eng.*, vol. 65, no. 9, pp. 1912–1923, Sep. 2018.

[51] A. Oliveira, S. Pereira, and C. A. Silva, "Retinal vessel segmentation based on fully convolutional neural networks," *Expert Syst. Appl.*, vol. 112, pp. 229–242, Dec. 2018.

[52] Y. Jiang, N. Tan, T. Peng, and H. Zhang, "Retinal vessels segmentation based on dilated multi-scale convolutional neural network," *IEEE Access*, vol. 7, pp. 76342–76352, 2019.
[53] J. Zhang, B. Dashtbozorg, E. Bekkers, J. P. W. Pluim, R. Duits, and B. M. ter Haar Romeny, "Robust retinal vessel segmentation via locally adaptive derivative frames in orientation scores," *IEEE Trans. Med. Imag.*, vol. 35, no. 12, pp. 2631–2644, Dec. 2016.
[54] P. K. Karn, B. Biswal, and S. R. Samantaray, "Robust retinal blood vessel segmentation using hybrid active contour model," *IET Image Process.*, vol. 13, no. 3, pp. 440–450, Feb. 2019.
[55] U. T. V. Nguyen, A. Bhuiyan, L. A. F. Park, and K. Ramamohanarao, "An effective retinal blood vessel segmentation method using multi-scale line detection," *Pattern Recognit.*, vol. 46, no. 3, pp. 703–715, Mar. 2013.
[56] S. Chaudhuri, S. Chatterjee, N. Katz, M. Nelson, and M. Goldbaum, "Detection of blood vessels in retinal images using two-dimensional matched filters," *IEEE Trans. Med. Imag.*, vol. 8, no. 3, pp. 263–269, 1989.
[57] X. Jiang and D. Mojon, "Adaptive local thresholding by verification-based multithreshold probing with application to vessel detection in retinal images," *IEEE Trans. Pattern Anal. Mach. Intell.*, vol. 25, no. 1, pp. 131–137, Jan. 2003.
[58] F. Zana and J.-C. Klein, "Segmentation of vessel-like patterns using mathematical morphology and curvature evaluation," *IEEE Trans. Image Process.*, vol. 10, no. 7, pp. 1010–1019, Jul. 2001.
[59] M. E. Martinez-Perez, A. D. Hughes, S. A. Thom, A. A. Bharath, and K. H. Parker, "Segmentation of blood vessels from red-free and fluorescein retinal images," *Med. Image Anal.*, vol. 11, no. 1, pp. 47–61, Feb. 2007.
[60] G. Azzopardi, N. Strisciuglio, M. Vento, and N. Petkov, "Trainable COSFIRE filters for vessel delineation with application to retinal images," *Med. Image Anal.*, vol. 19, no. 1, pp. 46–57, Jan. 2015.
[61] Y. Zhao, L. Rada, K. Chen, S. P. Harding, and Y. Zheng, "Automated vessel segmentation using infinite perimeter active contour model with hybrid region information with application to retinal images," *IEEE Trans. Med. Imag.*, vol. 34, no. 9, pp. 1797–1807, Sep. 2015.
[62] M. Melinscak, P. Prentasic, and S. Loncaric, "Retinal vessel segmentation using deep neural networks," in *Proc. 10th Int. Conf. Comput. Vis. Theory Appl.*, 2015, pp. 1–6.
[63] T. A. Soomro, M. A. U. Khan, J. Gao, T. M. Khan, M. Paul, and N. Mir, "Automatic retinal vessel extraction algorithm," in *Proc. Int. Conf. Digit. Image Computing: Techn. Appl. (DICTA)*, Nov. 2016, pp. 1–8.
[64] M. A. U. Khan, T. A. Soomro, T. M. Khan, D. G. Bailey, J. Gao, and N. Mir, "Automatic retinal vessel extraction algorithm based on contrast-sensitive schemes," in *Proc. Int. Conf. Image Vis. Comput. New Zealand (IVCNZ)*, Nov. 2016, pp. 1–5.
[65] T. A. Soomro, M. A. U. Khan, J. Gao, T. M. Khan, and M. Paul, "Contrast normalization steps for increased sensitivity of a retinal image segmentation method," *Signal, Image Video Process.*, vol. 11, no. 8, pp. 1509–1517, Nov. 2017.
[66] T. A. Soomro, M. Paul, J. Gao, and L. Zheng, "Retinal blood vessel extraction method based on basic filtering schemes," in *Proc. IEEE Int. Conf. Image Process. (ICIP)*, Sep. 2017, pp. 4422–4426.
[67] T. A. Soomro, A. J. Afifi, J. Gao, O. Hellwich, M. A. U. Khan, M. Paul, and L. Zheng, "Boosting sensitivity of a retinal vessel segmentation algorithm with convolutional neural network," in *Proc. Int. Conf. Digit. Image Comput., Techn. Appl. (DICTA)*, Nov. 2017.
[68] T. A. Soomro, T. M. Khan, M. A. U. Khan, J. Gao, M. Paul, and L. Zheng, "Impact of ICA-based image enhancement technique on retinal blood vessels segmentation," *IEEE Access*, vol. 6, pp. 3524–3538, 2018.
[69] T. A. Soomro, A. J. Afifi, J. Gao, O. Hellwich, M. Paul, and L. Zheng, "Strided U-net model: Retinal vessels segmentation using dice loss," in *Proc. Digit. Image Comput., Techn. Appl. (DICTA)*, Dec. 2018, pp. 1–8.
[70] M. K. T. M. Khan and D. T. A. Bailey Soomro, "A generalized multi-scale line-detection method to boost retinal vessel segmentation sensitivity," *Pattern Anal. Appl.*, vol. 22, no. 3, pp. 1177–1196, 2018.
[71] T. A. Soomro, J. Gao, Z. Lihong, A. J. Afifi, S. Soomro, and M. Paul, "Retinal blood vessels extraction of challenging images," in *Data Mining* (Communications in Computer and Information Science), vol. 996, nos. 1–12. Singapore: Springer, 2019.
[72] T. A. Soomro, A. J. Afifi, A. Ali Shah, S. Soomro, G. A. Baloch, L. Zheng, M. Yin, and J. Gao, "Impact of image enhancement technique on CNN model for retinal blood vessels segmentation," *IEEE Access*, vol. 7, pp. 158183–158197, 2019.
[73] Y. Hou, "Automatic segmentation of retinal blood vessels based on improved multiscale line detection," *J. Comput. Sci. Eng.*, vol. 8, no. 2, pp. 119–128, Jun. 2014.

MOHAMMAD A. U. KHAN received the B.S. degree from UET Peshawar, Pakistan, in 1992, the M.Sc. degree from the Loughborough University of Technology, in 1994, and the Ph.D. degree from Georgia Tech, in 1999. Since 1999, he has been actively involved in image processing, pattern recognition, and machine learning. He published extensively in residual vector quantization, directional filterbank, retinal vessel extraction, and signature verification.

FAIZAN ABDULLAH received the B.S. degree from COMSATS University, Islamabad, and the master's degree in data analytics from Deakin University, Melbourne. He has been actively involved in image processing and artificial intelligence. He has published conferences and journal papers. He helped to perform the experiments and analysis of this article.

AWAIS AKRAM received the Bachelor of Medicine and Bachelor of Surgery (M.B.B.S.) degree from the University of Health Sciences, Lahore. He is currently working as a Medical Officer with the Primary and Secondary Health Care Department, Government of Pakistan. His research interests include diabetic retinopathy, hypertensive retinopathy, age related macular oedema, and retinitis pigmentosa.

RIZWAN ALI NAQVI received the B.S. degree in computer engineering from COMSATS University, Pakistan, in 2008, the M.S. degree in electrical engineering from Karlstad University, Sweden, in 2011, and the Ph.D. degree in electronics and electrical engineering from Dongguk University, South Korea, in 2018. From 2011 to 2012, he was a Lecturer with the Computer Science Department, Sharif College of Engineering and Technology, Pakistan. He joined the Faculty of Engineering and Technology, The Superior College, Pakistan, as a Senior Lecturer, in 2012. From 2018 to 2019, he worked as a Postdoctoral Researcher with Gachon University, South Korea. He is currently working as an Assistant Professor with Sejong University, South Korea. His research interests include gaze tracking, biometrics, computer vision, artificial intelligence, machine learning, deep learning, and medical imaging analysis.

MEHWISH MEHMOOD received the B.S. and M.S. degrees in electrical engineering from COMSATS University, Islamabad, Pakistan, in 2015 and 2018, respectively. From 2016 to 2018, she was a Research Associate with COMSATS University. She is currently working as a Laboratory Engineer with COMSATS University. Her research interests include image processing, machine learning, and computer vision.

DILDAR HUSSAIN received the B.S. degree in computer science from the Kohat University of Science and Technology, Pakistan, in 2010, and the Ph.D. degree in biomedical engineering from Kyung Hee University, South Korea, in 2019. From 2013 to 2019, he worked as a Research and Development Engineer with YOZMA BMTech Company Ltd., South Korea (develop diagnostic imaging equipment instruments i.e., DXA, Chats X-rays, and Ultrasonic). He is currently working as a Postdoctoral Research Fellow with the School of Computational Science, Korea Institute for Advanced Study (KIAS), which is a subordinate institute of KAIST, South Korea. His research interests include bioinformatics, medical imaging, medical image analysis, computer vision, biomedical natural image processing, artificial intelligence, machine learning, deep learning, mineral, and nutritional study.

TOUFIQUE AHMED SOOMRO (Member, IEEE) received the B.E. degree in electronic engineering from the Mehran University of Engineering and Technology, Pakistan, in 2008, the M.Sc. degree in electrical and electronic engineering by Research from the University Technologi PETRONAS, Malaysia, in 2014, and the Ph.D. degree in AI and image processing from the School of Computing and Mathematics, Charles Sturt University, Australia. He remained as a Research Assistant for a period of six months with the School of Business Analytic in Cluster of Big Data Analysis, University of Sydney, Australia. He is currently an Assistant Professor with the Electronic Engineering Department, QUEST, Larkana, Pakistan. His research interests include most aspects of image enhancement methods, segmentation methods, and classifications methods and image analysis for medical images.